Understanding the lattice composition directed *in situ* structural disorder for enhanced visible light photocatalytic activity in Bismuth iron niobate pyrochlore

R. Radha, Y. Ravi Kumar, M. Sakar, K. Rohith Vinod, S. Balakumar*

National Centre for Nanoscience and Nanotechnology, University of Madras, Guindy Campus, Chennai 600025, India

A B S T R A C T

Herein we report the cationic disorder dependent photocatalytic efficiency of pyrochlore type $Bi_{1.33}$ $Fe_{0.052}Nb_{1.24}Fe_{1.04}O_{7-\delta}$ (BFNF) and $Bi_{1.34}Fe_{0.66}Nb_{1.34}O_{7-\delta}$ (BFN) nanoparticles (Nps) for the first time. Bi based photocatalytic materials endowed with lone pair of $6s^2$ electrons is additionally perturbed by nonstoichiometry and studied for its optoelectronic properties. Rietveld refinements show that the crystal structure is cubic and the space group is Fd$\bar{3}$m. In BFNF Nps, Bi^{3+} cation on the eight coordinate pyrochlore A-site shows displacive disorder, as a consequence of its lone pair electronic configuration as well as due to higher iron concentration. The lattice vibrational analysis using Raman spectra is consistent with the displacive disorder of the pyrochlore. A quantitative chemical compositional and state analysis has been done using X-ray photoelectron spectroscopy. The band-gap energy (Eg) and band edge offset of BFNF and BFN NPs were estimated to be 2.43 and 2.56 eV respectively by using UV–vis spectroscopy and the valence band XPS spectra. Under visible light, the BFNF NPs exhibits a much better visible-light-responsive photocatalytic performance than BFN NPs for the degradation of RhB and commercially available pharmaceutical acetoaminophen (Dolo 650). The mechanism of high photo-catalytic activity was suggested on the basis of the photoluminescence spectra, electrochemical impedance spectra (EIS), and active species trapping measurements. Our findings indicated that the synergistic effect of higher degree of cationic disorder in BFNF NPs is responsible for favourable direct transition along with NBE (near bandedge) transition, efficient separation and migration of photoinduced charge carriers, thus resulting in the remarkably improved photocatalytic activity.

1. Introduction

Addressing today's environmental crisis, one such possible solution is photocatalytic semiconductors based on nanotechnology, which have drawn considerable focus, due to their unique physicochemical properties. Away from TiO_2, in order to achieve high energy conversion efficiency, Bi-based compounds have attracted considerable attention as the Bi $6s^2$ lone pair of electron endows the Bi-related compounds with the stereochemical activity as well as the intrinsic polarization. This plays a crucial role in the surface valence fluctuation and modification of the charge distribution in the metal-oxide bonds [1]. Consequently, Bi based photocatalytic materials has been widely reported in literature that broadly include ferrite ($BiFeO_3$) [2], titanate ($Bi_2Ti_2O_7$) [3], tungstate ($BiFeWO_6$) [4], vanadate ($BiVO_4$) [5], niobate (Bi_2FeNbO_7) [6], of which pyrochlore structured material offers band gap in the visible region and a manipulative crystal structure that can be desired for developing an ideal photocatalyst [7]. These pyrochlore structured materials with general chemical formula $A_2B_2O_7$, grab attention, as they offer the ability to manipulate electron/hole mobility by the choice of different elements introduced in different sites [8]. Also, the combinational variations made in 'A', 'B', and oxygen sites and in structural parameters such as bond length, bond angle together contribute in the electronic structure influencing the photocatalytic behaviour [9,10]. Recently, many pyrochlore-type Bi based compounds ($A_2B_2O_7$) have been studied to evaluate their semiconductor properties for photocatalytic applications such as $Bi_2Ti_2O_7$ [11,12], $Pb_2Nb_2O_7$ [13], Fe_2BiSbO_7 [14], $Bi_2Zr_2O_7$ [15], other pyrochlore compounds that have been reported as rare earths are Sm_2FeTaO_7 [16], $Tm_2Ti_2O_7$ [17], $Bi_2Ce_2O_7$ [18], and $Ln_2Ti_2O_7$ (Ln = Nd, Gd, Er) [19]. Among these, Bi-based pyrochlores with general formula $Bi_2(M^{III}Nb^V)O_7$ is well known for its inconceivable electronic properties in photocatalytic applications [20]. A wide range of compounds Bi_2MNbO_7 (M = Al, Fe, Ga, In) were studied for water decomposition [21]. Notably, the iron containing compound Bi_2FeNbO_7 shows promising electronic and catalytic

performance [22,23]. The crystallography and chemistry of this compound is quite interesting because of two reasons: Firstly, they exhibit significant short-range disorder due to the displacement of Bi^{3+} cations and O^- anions from their ideal positions, resulting due to stereochemically active $6s^2$ electron lone pair on Bi^{3+}. Secondly, they have been shown to be slightly nonstoichiometric, with 5% Fe^{3+} doping for Bi^{3+} on the A site and a similar Fe^{3+} excess on the mixed Fe^{3+}/Nb^{5+} B site (the latter leading to vacancies on the O' site) [20]. Lufaso et al. has claimed that a compound with the composition Bi_2FeNbO_7 does not actually exist, but rather forms a three-phase mixture of Bi_3NbO_7, $Bi_3Fe_{0.5}Nb_{1.5}O_9$ and a member of the A-site deficient Bi–Fe–Nb–O pyrochlore homogeneity range [24]. Recently Bencina et al. reported the higher photocatalytic efficiency of $Bi_{1.647}Nb_{1.118}Fe_{1.157}O_7$ nanoparticle than that of TiO_2, due to the harness of longer wavelength light for photocatalysis [25]. Miller et al. has reported the influence of local structural disorder on the magnetic property of $Bi_{1.89}Fe_{1.16}Nb_{0.95}O_{6.95}$ [20]. Studies of the local structure of Bi-Zn/Fe-Nb-O pyrochlores by Krayzman et al. [26] revealed that the displacement directions of the A-site ions are determined by nature of A-site cations and the local B-site configurations. Avdeev et al. [27] noted that the off-centering of the A-site cations occurs when the A-site is occupied by small transition metal ions, as the A-site cavity is large for them to maintain the ideal central position. Thus it is understood that the structural disorder in Bi-Fe-Nb-O compounds can be induced by varying the cation ratio. Consequently this provoked the idea to study the visible light photocatalytic efficiency of varied ratio of Bi, Fe and Nb atoms in the lattice of the Bi-Fe-Nb-O pyrochlore nanoparticles.

However there are number of reports available relating to the structural disorder and physical properties of the material, but our work is intended to shed light on the potential relation among nonstoichiometry, structural disorder and photocatalytic efficiency of a visible light driven photocatalyst [28,29]. Thus the nanoparticles of thermodynamically stable phase of different molar ratio of Bi-Fe-Nb-O solid solutions were synthesized by a facile co-precipitation method. This study reports their structural, morphological, optical properties and compares the photocatalytic efficiency of ideal pyrochlore and disordered pyrochlore of Bi-Fe-Nb-O solid solution.

2. Materials and methods

2.1. Materials

All the chemicals used for the study were of analytical grade without any further purification. Bismuth nitrate (Alfa Aesar), ferric nitrate (Merck), niobium chloride (Merck), ammonia solution (Chemspure), nitric acid (Rankem) and methylene blue (Fisher Chemicals) were used.

2.2. Methods

2.2.1. Photocatalyst synthesis

The BFNF and BFN NPs were synthesized through a facile co-precipitation method. In the typical synthesis process, $Bi(NO_3)_3 \cdot 5H_2O$, $Fe(NO_3)_3 \cdot 9H_2O$ and $NbCl_5$ were taken in a molar ratio of 4:3:3 and 2:1:1 respectively for BFNF and BFN nanoparticle synthesis. Correspondingly, they were dissolved in double distilled water and magnetically stirred for 30 min individually. Later a transparent homogenous solution was obtained by mixing all the three precursors. The pH was adjusted to 1, by adding HCl appropriately. The final product was precipitated by adding the required amount of NH_4OH solution. The precipitate was collected and washed several times using ethanol and double distilled water and dried at 100 °C for 3 h in a hot air oven. Then, the dried as-prepared powder was annealed at 550, 600, 650 and 700 °C for 6 h to obtain the phase of the material.

2.2.2. Characterisation techniques

The synthesized materials were characterized for their structural properties using X-ray diffraction technique (XRD-PANalytical Instruments) and Raman spectroscopy (Raman 11 Nanophoton Corporation, Japan). The chemical state analysis were studied using X-ray photoelectron spectroscopy (XPS-Scienta Omicron Nanotechnologies) and so morphological and surface analysis using field emission scanning electron microscope (FESEM-Hitachi High Tech SU6600), high resolution transmission electron microscope (HRTEM-Techni G2S TWIN, FEI) and porosimeter (ASAP2020 from Micromeritics) were performed. The optical characterisations were done using UV–visible absorption/diffuse reflectance spectroscopy (UV–vis Abs/DRS-PerkinElmer) and photoluminescence spectroscopy (PL-HORIBA Jobin Yvons Lab- RAM systems) techniques. The photocatalytic studies were carried out using a commercial photoreactor (HEBER Photoreactor, India) and photo electrical studies were done using electrochemical Impedance (VSP-300 multichannel potentiostat/ galvanostat, Bio-Logic Science Instruments, France).

2.2.3. Photocatalytic activity

The photocatalytic efficiency of BFNF and BFN NPs was delved over the degradation of the heteropolyaromatic dye-rhodamine B (RhB). In a typical experiment, 10 mg of RhB dye was dissolved in 1000 ml of water, of which 100 ml was isolated and tested for degradation. 100 mg of BFNF and BFN NPs were dispersed in 100 ml of RhB solution separately. Before exposure, the suspensions were stirred in dark for 30 min to ensure the establishment of adsorption/desorption equilibrium of RhB on the sample surfaces. The suspensions were then exposed to direct irradiation of visible light (300 W tungsten lamp). Consequently 5 ml of suspension at regular time interval were centrifuged at a rate of 6000 rpm for 10 min. Photodegradation of RhB dye, which has characteristic absorption peak at 554 nm was monitored by UV–vis absorption spectra obtained by using Perkin Elmer Lambda 650s spectrophotometer. A similar procedure was followed for visible light photodegradation of acetoaminophen (DOLO 650), to rule out the possibility of dye sensitization of RhB, where acetoaminophen has absorbance at 243 nm.

To detect the active species generated in the photocatalytic process, disodium ethylene diamine tetraacetate (EDTA-2Na), isopropanol (IPA), and 1,4-benzoquinone (BQ) were chosen as the hole (h^+), hydroxyl radical ($\cdot OH$), and superoxide radical ($\cdot O^{2-}$) scavengers, respectively. Typically, 50 mg of photocatalyst with different scavengers (1 mmol) were ultrasonically dispersed in RhB aqueous solution (50 ml, 3 ppm), and the following processes were similar to the above photodegradation experiment. The electrochemical impedance spectroscopy (EIS) measurments were performed, in the presence of 5.0 mM $K_3[Fe(CN)_6]/K_4[Fe(CN)_6]$ by applying an AC voltage with 5 mV amplitude in a frequency range from 1 Hz to 85 kHz under open circuit potential conditions.

3. Results and discussion

3.1. Crystal structure and phase analysis

The XRD patterns of the obtained Bi-Fe-Nb-O system annealed at different temperatures of both BFN and BFNF Nps are shown in Fig.S1 (a & b) in ESI. The obtained peaks of BFN and BFNF Nps are found to be matched with that of JCPDS data (card #52-1774) adopting cubic pyrochlore structure ($A_2B_2O_7$) in space group $Fd\bar{3}m$. It is noteworthy that the phase formation temperature are different for the samples, BFNF is phase pure at 650 °C, while BFN Nps are phase pure at 600 °C that implies the requirement of excess of heat to accommodate the additional Fe ions into the lattice. However, the lattice composition of the formed phases has been expected to be different as per the amount of precursors taken, which is precisely revealed from the Rietveld refinement studies of the samples. Fig. 1(a)–(b) shows the obtained
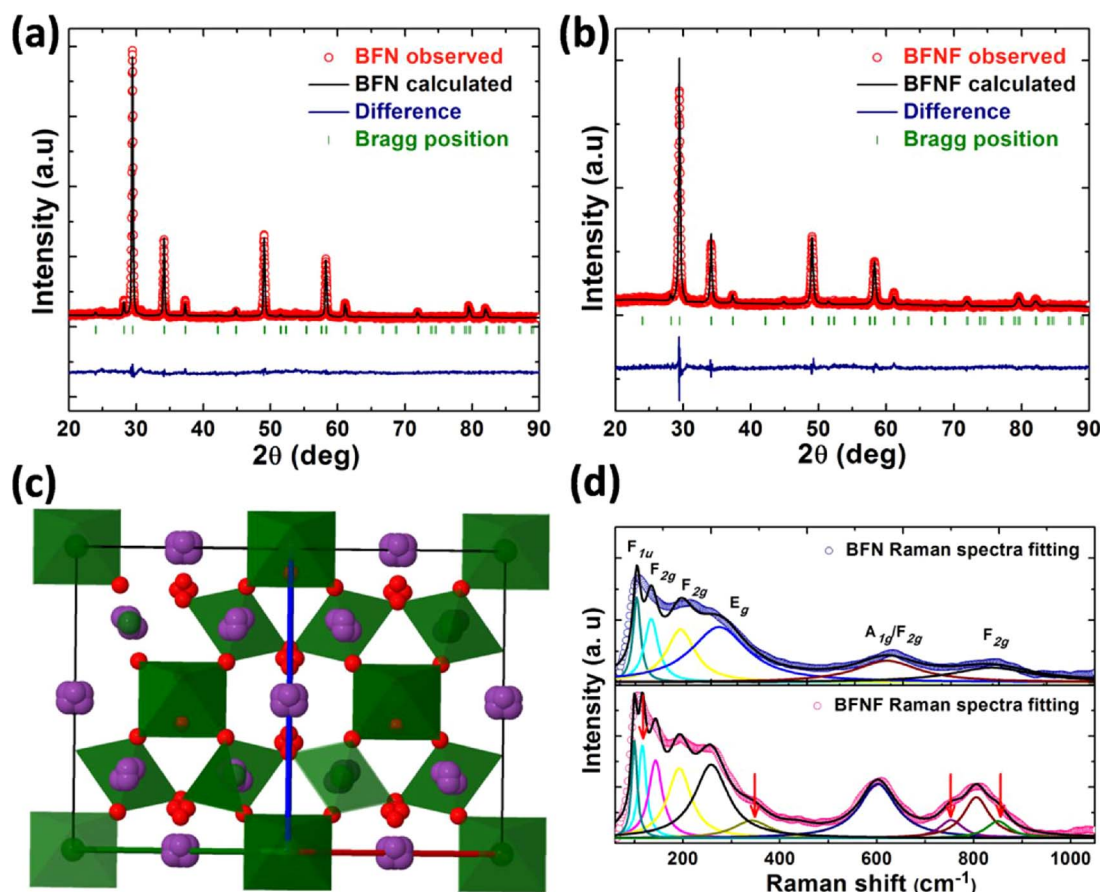
Fig. 1. *(a & b)* Observed (circles), calculated (solid line) and difference (below) XRD profiles of BFNF (a) and BFN (b) taken at room temperature using Cu K_α radiation, *(c)* BFNF Crystal structure of the displacively disordered pyrochlore 0.4400:0.2700:0.2900 Bi_2O_3:Fe_2O_3:Nb_2O_5 according to the Rietveld refinement results given in Table 1. The vertex-linked polyhedra represent the octahedral B_2O_6 ¼ $(Fe,Nb)_2O_6$ network. Bi/Fe sites are purple (light grey) ellipsoids forming disordered distorted hexagons; and O atoms are red ellipsoids with the O'sites forming disordered tetrahedra. and *(d)* Sum of Lorentzian curves fit of the Raman spectra of BFNF and BFN Nps. Experimentally measured spectra (black), fitted curve (open circles), baseline (black).

refined XRD patterns of BFN and BFNF using FULPROF algorithm. The interplay of constituted elements due to their population in the composition plays crucial roles in creating the disordered pyrochlore structures. Such scenario can be evidently found in the case of bismuth ferrite, where the excess bismuth precursor taken essentially resists the formation of any secondary phases in $BiFeO_3$. Similarly, as per the amount of precursors taken in such way that Bi: Fe: Nb is 2:1:1 and 4:3:3 that yielded a Bi-Fe-Nb-O system with two different lattice composition such as $Bi_{1.34}Fe_{0.66}Nb_{1.34}O_{7-\delta}$ (BFN) and $Bi_{1.33}Fe_{0.052}Nb_{1.24}Fe_{1.04}O_{7-\delta}$ (BFNF), respectively. Refinement of BFN phase with Bi at 96 g and O' at 8b resulted $\chi^2 = 1.502$ and $R_{wp} = 8.2215$, which depicts the cubic pyrochlore structure, but under similar parameters when employed for BFNF phase resulted in discrepancies in thermal values and χ^2 values. In the next step, smaller Fe^{3+} was allowed to occupy A site and later O' was assigned to 32e site for refinement. This misplaced displacive model taken for refinement resulted $\chi^2 = 2.337$ and $R_{wp} = 8.6167$ with better thermal values. Any other choice of O' position worsened the refinement. The Rietveld refined positional, thermal and occupancy parameters are shown in Table 1.

The general chemical formula of this pyrochlore structure is $A_2B_2O_6O'$, where it should be noted that the off-stoichiometric ratio of the precursors taken (4:3:3) as compare to the ideal stoichiometric ratio (2:1:1), the excess Fe (B site) taken, with respect to Bi, occupies the Bi site up to 4% to 15% [4,27]. Therefore, the off-stoichiometric leads to the formation of $Bi_{1.33}Fe_{0.052}Nb_{1.24}Fe_{1.04}O_{7-\delta}$ phase (BFNF). The existing reports emphasize that the stoichiometric pyrochlore structure in Bi-M-Nb-O, where M = Zn, Mn and Cu, is formed when the

concentration of Bi atoms is relatively higher with respect to M-Nb atoms [30–32].

At any given lower concentration of A-site atoms, the induced cationic deficiency in A-sites would be occupied by the B-site atoms as to create charge balance in these pyrochlore structures. Accordingly, the Rietveld refinements on the XRD pattern of BFN and BFNF revealed that the formation of displaced pyrochlore (BFNF) phase as obtained by Lufaso et al., in which the A-site atoms are displaced to 96 g sites and the O' atoms are displaced to 32e sites [24,33]. The refinement parameters of BFN phase using the conventional model for $A_2B_2O_6O'$ pyrochlore with the space group $Fd\bar{3}m$ (227) and four crystallographic-independent atom sites, where A (Bi) in 16d at (1/2, 1/2, 1/2); B (Fe/Nb) in 16c at (0, 0, 0); O in 48f at (x, 1/8, 1/8), and O' in 8b at (1/8, 1/8, 1/8) is in good agreement with an ideal $A_2B_2O_6O'$ pyrochlore structure. However, the refinements of BFNF showed the occurrence of large atomic displacements in A-sites due to the presence both Bi as well as Fe atoms and O' atoms, which creates a static disorder in the material as shown in Fig. 1(c). This type of static disorders can be explained by the stereochemically active $6s^2$ electron lone pair in Bi^{3+} ions, which has been previously reported in $Bi_2Ru_2O_7$ by Avdeev et al. and eventually a large number of Bi-based pyrochlores have been studied in this field [27,34].

The obtained parameters revealed that the O' ions that are located at 8b site in BFN phase has been displaced to 32e site in BFNF phase with a displacement distance of 0.13 Å. Thereby, this shows about 6% of A-sites (Bi) atoms are occupied by Fe atoms and therefore the displace of B-site atoms (Fe) to the A-site (Bi) in this pyrochlore structures is inevitable in order to move the O' ions to achieve the chemically

Table 1

Final Rietveld refinement results for pyrochlore-type 0.4400:0.2700:0.2900 BFNF and 1.34:0.66:1.34 BFN – Bi_2O_3:Fe_2O_3:Nb_2O_5 nanoparticles.

Parameters	BFNF		BFN	
	Unit cell parameters			
Space group	Fd-3m		Fd-3m	
a = b = c	10.50223 Å		10.4940(11) Å	
α = β = γ	90°		90°	
Volume	1158.36230 Å³		1155.645 Å³	
	Atomic position and occupancy			
	Atomic position (x,y,z)	Occupancy	Atomic position (x,y,z)	Occupancy
Bi/Fe	(0.48339, 0.51486, 0.51639)	0.2788(6)/ 0.01084	(0.5, 0.5, 0.5)	0.3174(2)
Nb/Fe	0.48339, 0.51486, 0.51639	0.51887/ 0.43511	0.48339, 0.51486, 0.51639	0.2035(1)/ 0.2468(5)
O	(0.32998, 0.12500, 0.12500)	1.0000	(0.4174(80), 0.125, 0.125)	1.0000
O'	(0.38887, 0.38887, 0.38887)	0.46304	(0.3750, 0.3750, 0.3750)	0.3514(70)
	Refinement paramenters			
χ^2	2.337		1.502	
R_p	6.2436		6.5548	
R_{wp}	8.6167		8.2215	
R_{exp}	5.3347		6.7159	

reasonable bond distances [35]. These observations have also been reported in other systems, which are essentially demonstrated the correlation of displaced O' ions and A-site occupancy of smaller ions (*e.g.*, Fe, Co and Zn) [36,24]. Hence the site occupancy mediated compositional formulation of these pyrochlore compounds has been identified to be $Bi_{1.33}Fe_{0.052}Nb_{1.24}Fe_{1.04}O_{7-\delta}$ and $Bi_{1.34}Fe_{0.66}Nb_{1.34}O_{7-\delta}$.

It is noteworthy that the calculated lattice constant and cell volume show an increasing trend with increasing Fe cations in BFNF. Therefore, it is evident that $Bi_{1.34}Fe_{0.66}Nb_{1.34}O_{7-\delta}$ (BFN) possesses an ideal pyrochlore structure, while $Bi_{1.33}Fe_{0.052}Nb_{1.24}Fe_{1.04}O_{7-\delta}$ (BFNF) possesses a disordered pyrochlore structure with around 4% of Fe ions occupied in the A-site of Bi-Fe-Nb-O system.

3.2. Disorder studies using Raman spectra

The Raman spectra of BFN and BFNF phases with deconvoluted fittings are shown in Fig. 1(d), respectively. It is reported that a cubic Fd$\bar{3}$m ideal pyrochlore structure (*i.e.* a pyrochlore structure without any displacements of A-site and O' atoms from their ideal positions) exhibits six Raman active vibrations ($A_{1g} + E_g + 4F_{2g}$), seven F_{1u} infrared-active vibrations and one F_{1u} acoustic vibrations [34].

In such ideal pyrochlore structure, the Raman signals will be emerged only due to the B_2O_6 sublattice, whereas in a displaced pyrochlore structure, the relaxation of selection rules allow the emergence of more number of Raman signals including some infrared vibration signals [26]. The Raman spectra as shown in Fig. 1(d) can be divided into three groups such as low range (50–200 cm^{-1}), mid range (210–400 cm^{-1}), and high range (410–850 cm^{-1}) wavenumber regions. In the low range wavenumber region of BFNF NPs, the observed signal at 98.2 cm^{-1} can be assigned to F_{1u} infrared vibrations (O'–A–O' bend and A-BO$_6$) that emerge due to the relaxation of selection rules by the displacements of Bi and O' atoms from their ideal position. Similarly, the peaks at 144.4 and 193.2 cm^{-1} can be assigned to F_{2g} vibrations. However, it should be noted that the sharp peak at

257.2 cm^{-1} that corresponds to E_g vibrations for BFNF phase and the appearance of new unknown peak at 342.2 cm^{-1} (red arrow) for the BFNF phase could be attributed to the vibration that emerged due to the disorders in A-site occupancies. Such cases have also been reported in the literatures, where the Raman signals that are not appeared in the low range wavenumber in ideal pyrochlore consistently appeared in the bismuth based pyrochlore structure due to their displaced A-site atoms and associated displacement of the other atoms such as O' as well. [27] The signals in the high range wavenumber are predominantly due to the vibration of BO$_6$ octahedral sitting with vibration of 601.6 cm^{-1} corresponding to A_{1g}/F_{2g} mode. The deconvoluted peaks at 753 and 850.8 cm^{-1} (red arrows) in BFNF phase represent the unknown modes, which may be associated with modification induced in B–O stretch due to the disorder characteristic of the BFNF phase. Further, it is generally found to be that the signals that observed above 700 cm^{-1} are due to the overtones exclusively in the bismuth pyrochlores and the peak at 804.4 cm^{-1} may be assigned to the highest F_{2g} vibration which is found to be pronounced for the disordered BFNF phase as compare to the ideal BFN phase [22].

The salient outcome from the Raman analysis is realized to be that the high number of Raman vibrations (including deconvoluted peaks) of BFNF pyrochlore can be hardly assigned to a cubic pyrochlore with an ideal sitting of atoms in the respective sites. These vibrations essentially appear as a consequence of the relaxation of selection rules found by affecting the cell symmetry due to the induced displacive disorder in the BFNF pyrochlore, as evidenced in the Rietveld refinement results reported in this study.

3.3. Chemical state and compositional analysis using XPS spectra

The XPS investigation of BFNF NPs was performed to evaluate the chemical composition and the state of the constituted atoms. The peak position of different atoms was precisely determined by referencing the adventitious carbon at a binding energy of 284.6 eV. Wide range survey spectrum shown in Fig. 2(a), reveals no surface impurities. The atomic composition $Bi_{1.42}Fe_{1.04}Nb_{1.16}O_{7-\delta}$ calculated from the respective strong emission peaks Bi, Fe, Nb and O, clearly depicts that the higher Fe content in the lattice of BFNF NPs are in 4:3:3 ratios. The higher resolution spectra of Bi 4f in Fig. 2(b) deconvoluted to two doublets, suggests the presence of Bi^{3+} and Bi^{2+} [37]. From Fig. 2(d) the higher resolution spectra Fe 2p can be fitted as two peaks with binding energies of 712.8 eV and 725.5 eV, which are assigned to Fe $2p_{1/2}$ and Fe $2p_{3/2}$ respectively. Similarly from Fig. 2(c) the Nb 3d spectra can be best described with two doublets albeit of dramatically different half width. Considering the Nb $3d_{3/2}$ (209.4 eV) and Nb $3d_{5/2}$ (206.7 eV) suggest the chemical state of Nb^{3+} and the Nb 3d doublet with lesser binding energy correspond to Nb^{4+}. This disproportional distribution of Nb features the high concentration and distribution of Fe in the A site of the lattice of pyrochlore structure which is well explained by Chehereh et al. [38] The O 1s core level spectra is deconvoluted to four peaks with binding energies 533.2 eV, 532.3 eV 530.4 eV and 529.5.4 eV, which can be attributed the adsorbed water molecules, hydroxyl (OH) and carbonate (CO_3^{2-}) species, lattice oxygen and to the oxygen vacancies respectively is shown in Fig. 2(e) [39,40]. Thus the outcome of XPS investigation are found to be consistent with the XRD and Raman results, clearly stating the higher concentration and distribution of Fe in the A site of the site.

3.4. Morphological analysis using FESEM and HRTEM micrographs

The particle morphology of BFNF and BFN observed by FESEM is shown in Fig. 3(a, b) and (e, f) respectively. It is evident from the images that the nanoparticle sizes around 20–50 nm possessing a distorted spherical morphology and are inhomogenously distributed with agglomeration. The formation of thermodynamically stable spherical morphology is possible in the co-precipitation method as the digestion
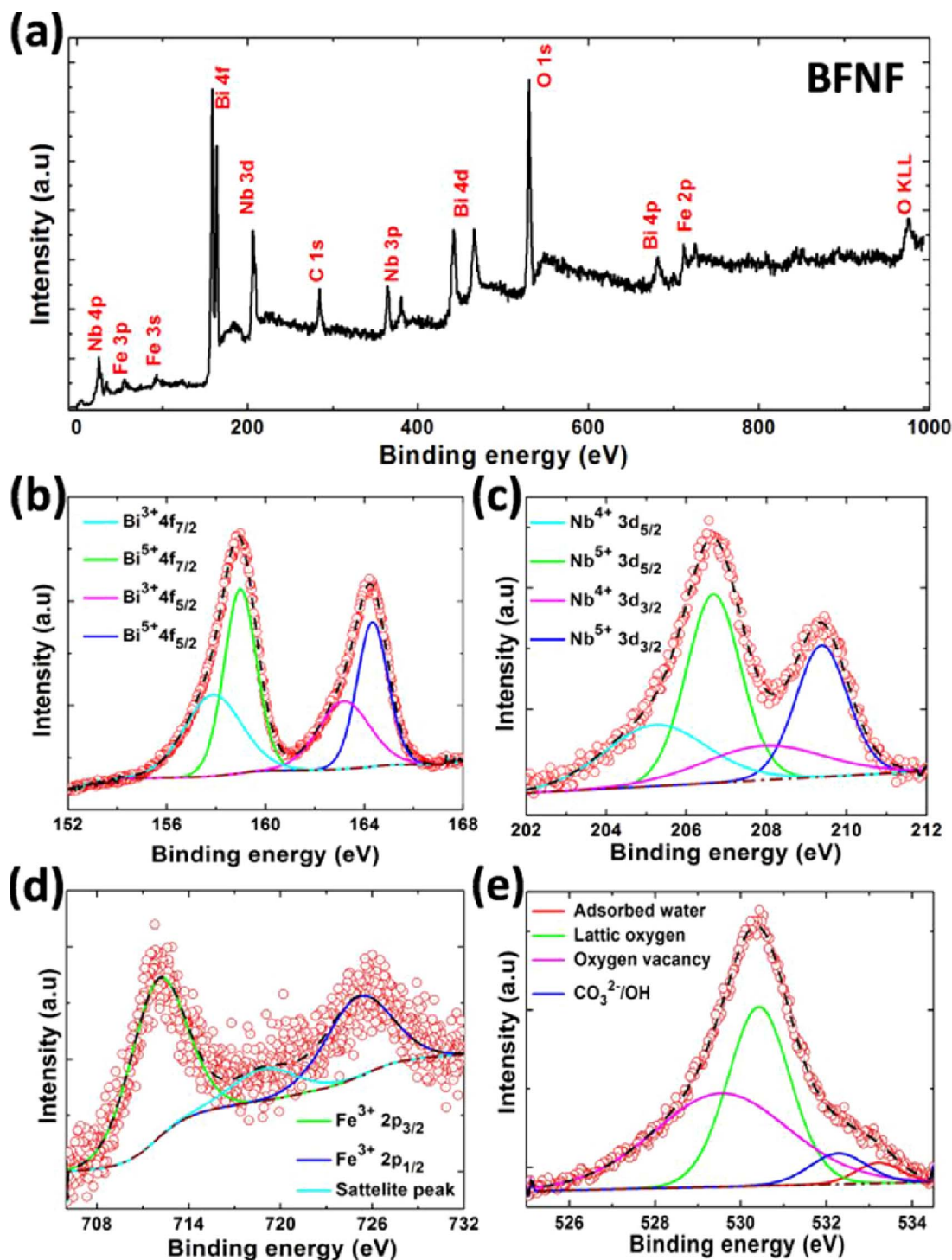
Fig. 2. (a) Survey spectrum, (b) Bi 4f, (c) Nb 3d (d) Fe 2p, and (e) O 1s XPS spectra of BFNF Nps.

of acidic solution with a base and formation of precipitation are likely a simultaneous process. Under such circumstances, the acidic nature of the solution controls the particle agglomeration and leads to the thermodynamically stable spherical morphology. The agglomerated clusters are originated from the sintering of nanometer-sized particles during the thermal treatment. HRTEM micrographs shown in Fig. 3(d & h) reveal the dimensions of the primary particles of around 80–110 nm for the both compositions. The inset of Fig. 3(c & g) shows the energy dispersive spectrum that qualitatively confirms the existence of Bi, Fe, Nb and O elements in the sample and no trace of any other elements. Quantitatively the atomic composition of BFNF and BFN Nps tabulated

in Table 2, are found to be consistent with $Bi_{1.33}Fe_{0.052}Nb_{1.24}Fe_{1.04}O_{7-\delta}$ and $Bi_{1.34}Fe_{0.66}Nb_{1.34}O_{7-\delta}$ composition.

3.5. Surface area analysis using BET studies

Particles in nanoregime are inevitable as the photocatalytic process is ultimately a surface reaction. In our case it is worth to have particles in nanodimension, yet in order to emphasis the potential relation between displacive disorder and photocatalytic efficiency, it is necessary to rule out the effect due to difference in the nano dimensional of the prepared BFNF and BFN Nps. Pan and co-workers has explained that the
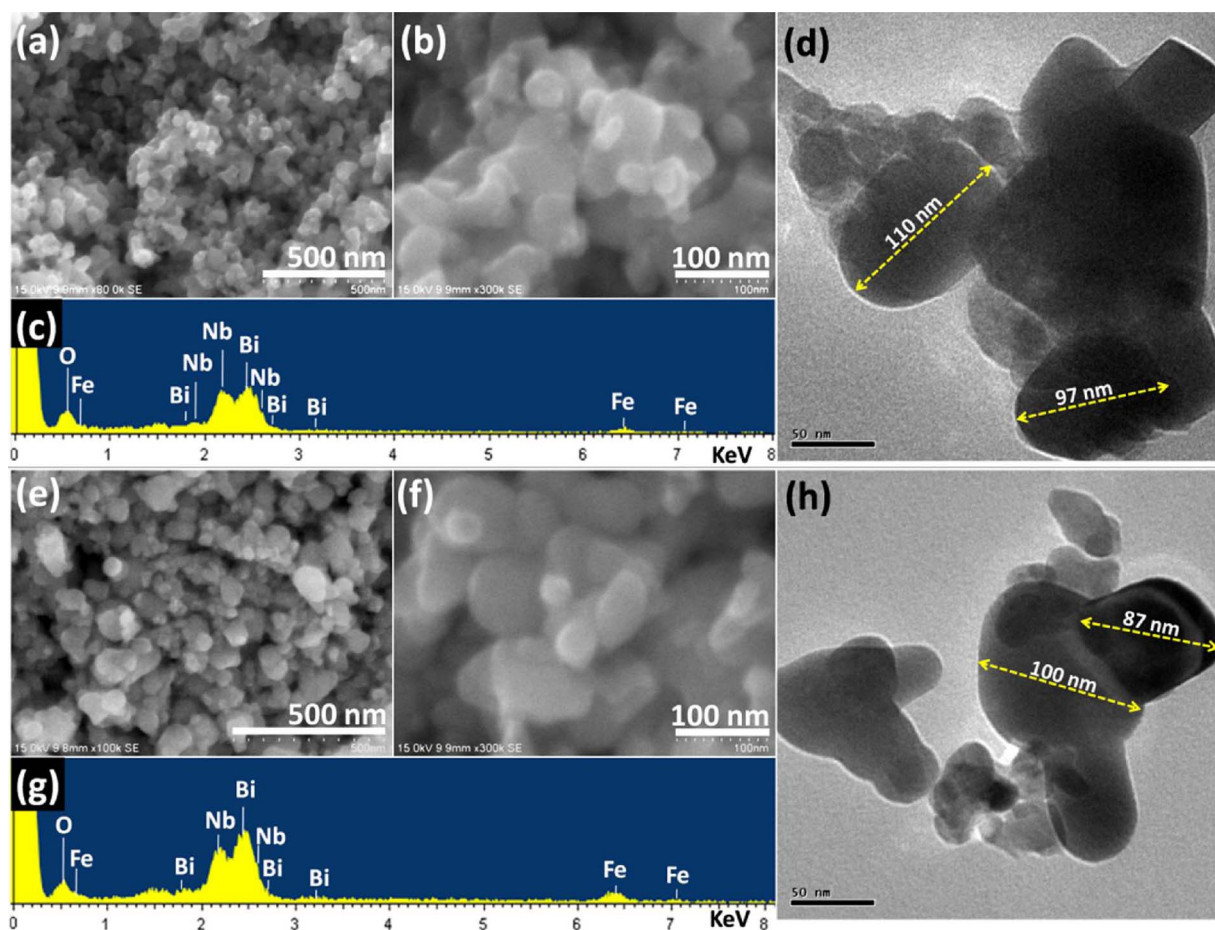
Fig. 3. (a, b) and (e, f)FESEM micrographs (c, g) EDS analysis and (d, h) HRTEM imagesof BFNF and BFN Nps revealing the spherical morphology.

Table 2
Elemental atomic composition of BFN and BFNF Nps.

Element	BFNF – Atomic%	BFN – Atomic%
Bi	15.01	12.70
Fe	12.55	5.46
Nb	14.43	9.82
Al	1.01	2.50
O	57	69.5

BET surface area greatly influences the catalytic activity [41]. Fig. 4(a & b) shows the N$_2$ adsorption–desorption isotherms of BFNF and BFN nanoparticles. The Brunauer–Emmett–Teller (BET) surface area analysis for BFNF and BFN Nps was found to be 16.8497 and 13.9391 m^2 g^{-1} respectively. It is noteworthy that the difference in the obtained surface area is negligible; hence the change in the photocatalytic efficiency may be attributed only to the structural change in BFNF Nps.

3.6. Optical property and mobility gap calculation

3.6.1. Energy band gap value using UV–vis DRS analysis

The optical properties were measured by UV–vis diffuse reflectance spectroscopy (DRS) in order realize the effect of disordered stereo-chemically active Bi 6s^2 lone pair of electrons. Fig. 5(a) shows the UV–visible DRS plot of the synthesised BFNF and BFN NPs. The lowest-energy indirect band gaps were measured for BFNF and BFN solid-solutions using Kubelka Munk plot is depicted in the inset of Fig. 5(a), a red-shift in the absorption edge of BFNF Nps is observed, and that may be attributed to the variation in the cationic composition which in turn has induced the structural disorder in BFNF Nps. A deeper insight on

the position of energy band edges in materials is essential to visualize the extent to which the structural modification has changed the optical property of BFNF rather than BFN Nps. Accordingly, the band edge energy of valence band (VB) is determined using XPS technique and the obtained spectra of BFNF and BFN Nps are shown in Fig. 5(b). It is obvious that there is shift in the VB of BFNF towards the lower energy region that may be attributed to asymmetric coordination of oxygen, as Lv et al. reported that the shallow oxygen-vacancy states would appear above and partly overlapping with VB [42]. Thus the asymmetric co-ordination of oxygen results due to occupancy of nearly 4% of Fe in Bi sites which imposes some of O' sites to be vacant in the lattice.

3.6.2. DOS analysis using XPS valence band spectra

A comparative picture of the density of states (DOS) of BFNF and BFN (Fig. 5(c)) can be determined from the UV–vis absorption results (Fig. 5(a)) and valance band (VB) XPS spectra (Fig. 5(b)). BFNF showed valence band DOS characteristics with the edge of the maximum energy at approximately ~0.0011 eV (Fig. 5(c)), whereas the valence band maximum energy of BFN was estimated to be ~0.31 eV. The optical band gap energy of BFNF and BFN Nps are ~2.46 eV and ~2.58 eV, respectively. Therefore, the conduction band (CB) minimum of BFNF and BFN Nps would occur at ~ −2.45 eV and ~ −2.29 eV, respectively. Thus, substantial band gap narrowing of the BFNF is a consequence of the shift of VB towards lower potential which is attributed to the displacement and/or substitution of Bi sites by Fe ions in the BFNF lattice system.

3.6.3. Optical transition studies using photoluminescence spectra

In this work, the luminescence properties or rather the fate of the excitons in BFNF and BFN Nps have been investigated in detail. The
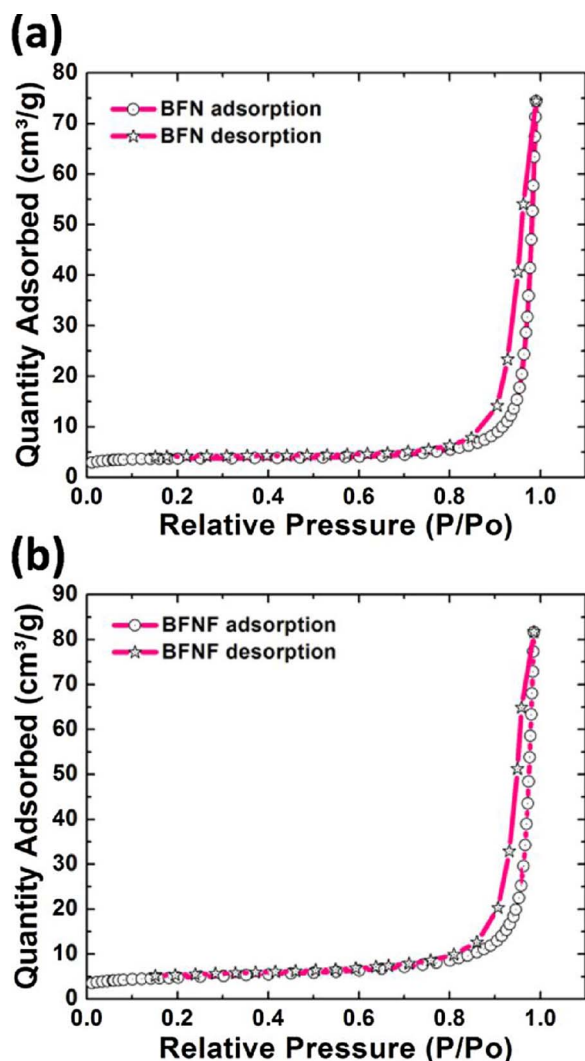
(a)

(b)

Fig. 4. N$_2$ gas adsorption–desorption isotherm of BFN (a) and BFNF (b) nanoparticles.

obtained PL spectra shows emission around UV region (312 nm) and in the visible region (466 nm), thus the simultaneous occurrence of both the emission may be attributed to its pyrochlore structure [43]. The use of different excitation wavelengths is useful in examining the luminescence spectra of materials containing multiple transition levels. It is also noteworthy that, with the increase of excitation wavelength, the position of peak of UV emission from BFNF shows significant red-shifts but the peak around 466 nm is stable, which is found to be the near band edge emission of BFNF, which is found in consistent with the UV DRS result. Hereby, it can be understood that the emission must be derived from multiple initial states to the same acceptor level that may be related to the asymmetric oxygen environment, rather than the same donor level to the VB, since the energy of emission should be either the same or absent under the latter condition. In case of Bi compounds, Bi 6s^2 lone pair of electrons, frequently used to rationalize the distorted local oxygen environment governs the electronic characteristic nature of the material [44]. Mohn. et al. has demonstrated that a disordered structure of Bi$_2$WO$_6$ possesses an unusual direct band gap at Γ, favourable in order to maximize the number of low-energy (direct) transitions, which is considered as an important aspect for the development of efficient photocatalysts [45]. Thus the observed direct transition in higher energy region and its red shift may be due to asymmetric local bismuth structure caused by the occupancy of Fe 3d cations on the A site. Additionally it can be noticed that the intensity of PL spectra of BFNF is comparatively less than BFN Nps in the visible

region which evidences the reduced recombination rate of the prepared BFNF Nps.

3.7. Photocatalytic activity analysis

3.7.1. Photoegradation of RhB and Acetoaminophen

The effects of the band gap reduction, a consequence of structural disorder on the photocatalytic degradation of the model organic pollutant RhB, a stable and is used frequently in the photochemical and textile industries, were examined under dark and visible light illumination conditions. A blank reaction without the catalyst in the light (Fig. S2 ESI) was conducted to determine the effects of the light on the dye solution. The organic pollutant RhB self-degradation under illumination conditions was almost negligible. Reaction with the catalyst in the dark and in the light was conducted to determine the effects of the light and dark conditions on the photocatalytic degradation of BFNF and BFN Nps. The degradation curves and the deduced C/C$_0$ ratio graphs are shown in Fig. 6(a)–(d).

It can be inferred that both the catalysts did not show activity under dark conditions. Moreover upon irradiation and in the given interval of time the BFNF Nps are found to effectively degrade the dye nearly 40% higher when compared to BFN Nps. The observed enhanced photocatalytic efficiency of BFNF Nps could be attributed to its distorted structure which has facilitated the following characteristics in BFNF Nps, (i) improved light absorption, (ii) increased photocurrent, (iii) effective charge separation and (iv) enhanced radical production. The recycling ability of the BFNF Nps after the catalytic reaction was observed by collecting, washing and drying the catalysts. The resulting photocatalyst showed the good stability after the five successive cyclic runs which further indicate its reusability.

It is noteworthy that in order to rule out the possibility of sensitivity of dye in the visible region, acetoaminophen (DOLO 650- paracetamol) a commercially available drug was used as pollutant which has absorbance in the UV region at 243 nm. A similar procedure was followed to monitor the efficiency of the samples, in which BFNF was found to be more efficient than BFN Nps and TiO$_2$ under similar irradiation. Fig. 7(a & b) shows the C/C$_0$ graph, from which it is understood is that BFNF Nps photodegrades ~95% of acetoaminophen in 180 min, while BFN and TiO$_2$ photodegrades only 50% and 40% respectively in the same interval. The Langmuir-Hinshelwood model was applied to quantitatively compare the reaction kinetics of the photo-degradation of the acetoaminophen. According to the model, the first order rate constant k is calculated by (C$_0$–C$_t$)/t, where C$_0$ is the initial concentration of the dye and C$_t$ is the concentration of the dye at the end of t time, which was taken as 180 min. The value of k for BFNF and BFN NPs are found to be 0.005213 and 0.002877 min^{-1} respectively, confirms the higher photocatalytic efficiency of BFNF NPs.

3.7.2. Scheme and photocatalytic mechanism

Based on the enhanced performance shown by BFNF Nps, the possible photo excitation of electrons and holes and its electronic transfer over the surface of photocatalysts under visible illumination was proposed, as depicted in Fig. 8. Compared to BFN, BFNF Nps exhibited remarkably enhanced photocatalytic activity under similar conditions. This significant difference in the activity of BFNF Nps depends on the crystalline nature with controlled particle size that facilitates the effective separation and migration of the photogenerated carriers in the photocatalyst [46]. First, when BFNF Nps was irradiated with visible light, it absorbs a wide range of wavelength, then photo excited electrons from the VB of BFNF migrate to the CB easily due to its sufficiently narrow band gap. Later these photoexcited electrons that are accumulated on the surface of BFNF Nps were then trapped by the dissolved oxygen molecules in water to yield superoxide radical anions ($\cdot O^{2-}$) and hydroxyl radicals (HO$\cdot$) [47]. Similarly, the photogenerated holes present on the surface of BFNF Nps react with the surface adsorbed hydroxyl ions to form highly reactive HO$\cdot$. These highly reactive
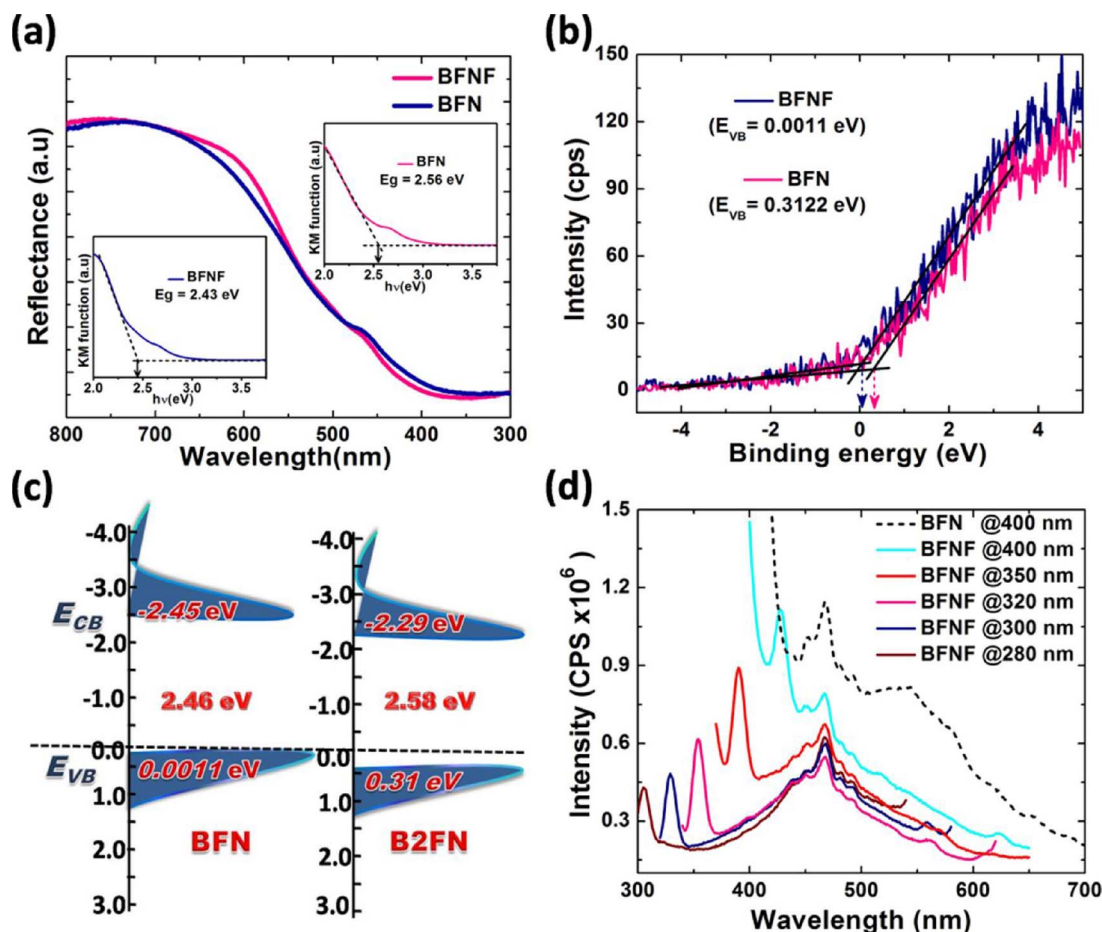
Fig. 5. (a) Comparative UV–vis diffuse reflectance spectra (b) Valence band XPS spectra (c) DOS characteristics (d) photoluminescence spectra at different excitation wavelength taken at room temperature of BFNF and BFN Nps.

radicals are responsible for the photodegradation and mineralization of organic pollutant RhB.

From the discussion about the optical properties of BFNF and BFN Nps it can be clearly deduced that BFNF Nps has wide absorbance, reduced band gap and favourable VB and CB position than that of BFN Nps. Thus the enhancement of the optical properties is a direct consequence of the static disorder pyrochlore structure that has been caused by the difference in the lattice composition of BFNF and BFN Nps. In a distorted environment coupling between the Bi 6s and 6p states occurs and the filled antibonding states are stabilized which leads to the formation of the lone pair. It has been reported that the activity of $BiVO_4$ arises from optical transitions between anti-bonding Bi 6s – O 2p orbitals at the top of the valence band and empty V 3d orbitals at the bottom of the conduction band. Moreover, the filled antibonding states at the top of the valence band are key to providing the shallow acceptor levels necessary for p-type conductivity [48]. In case of $Bi_2Sn_2O_7$ the presence of the structural distortion has a direct influence on the valence band position (ionisation potential), which in turn will influence the catalytic properties through the stability of electronic and ionic defects on the material surface [49]. Thus in our case XRD and Raman results suggest a higher degree of distortion in the pyrochlore structure of BFNF Nps than BFN Nps due to the occupancy of nearly 5% of Fe in Bi sites. The large A site cavities are occupied by smaller Fe ions which leads to the off centering of A sites and hence a higher degree of disorder. As suggested by Avdeev et al. this off centering may lead to the formation of high density of states near E_f. Recently a similar phenomena was reported, when the degree of distortion increased the dielectric constant increased in the electronic structure of $(Bi_{1.5}Zn_{0.5})$ $(Zn_{0.5}Nb_{1.5})O_7$. Consequently in BFNF Nps its optical transition

between antibonding 6s – O 2p is affected by the Fe 3d hydridisation, and is more pronounced than NBE (Near band edge) transitions in the visible region which is quite evident from the PL spectra results. These low energy direct transitions are favourable for the photocatalytic reaction to effectively take place. The filled antibonding states at the top of the VB and empty Nb 4d orbitals at the bottom of CB of BFNF Nps generates more number of excitons in the visible region than that of BFN. But the above said factors alone cannot ensure high photocatalytic activity because the separation of the photogenerated electron-hole pairs and their migration to the surface reaction sites to generate radicals also plays an important role in determining the photocatalytic performance. Thus, the ascribed enhanced carrier transportation and redox reactions of BFNF Nps were further validated through analyzing their photocurrent properties and their ability to generate radicals during the photocatalytic process.

3.7.3. Photoconductivity studies using electrochemical impedance spectra

EIS measurements were taken under dark and under illumination conditions to examine the interfacial characteristic of the prepared BFNF and BFN Nps-based photoelectrodes, such as charge transfer resistance and recombination rate of the photogenerated electrons-holes. The separation efficiency of photogenerated electron and hole pairs also plays a vital role in the enhancement of photocatalytic activity. Fig. 7(d) shows the EIS results of BFNF and BFN Nps, which reflects the smaller arc radius of BFNF when compared to the BFN Nps. In each case, there is one arc on the EIS plane, indicating that the surface charge transfer is the rate-determining step in the photocatalytic reaction. A necessary step for semiconductor photocatalytic performance is the generation and separation of photogenerated electron-hole pairs. Both
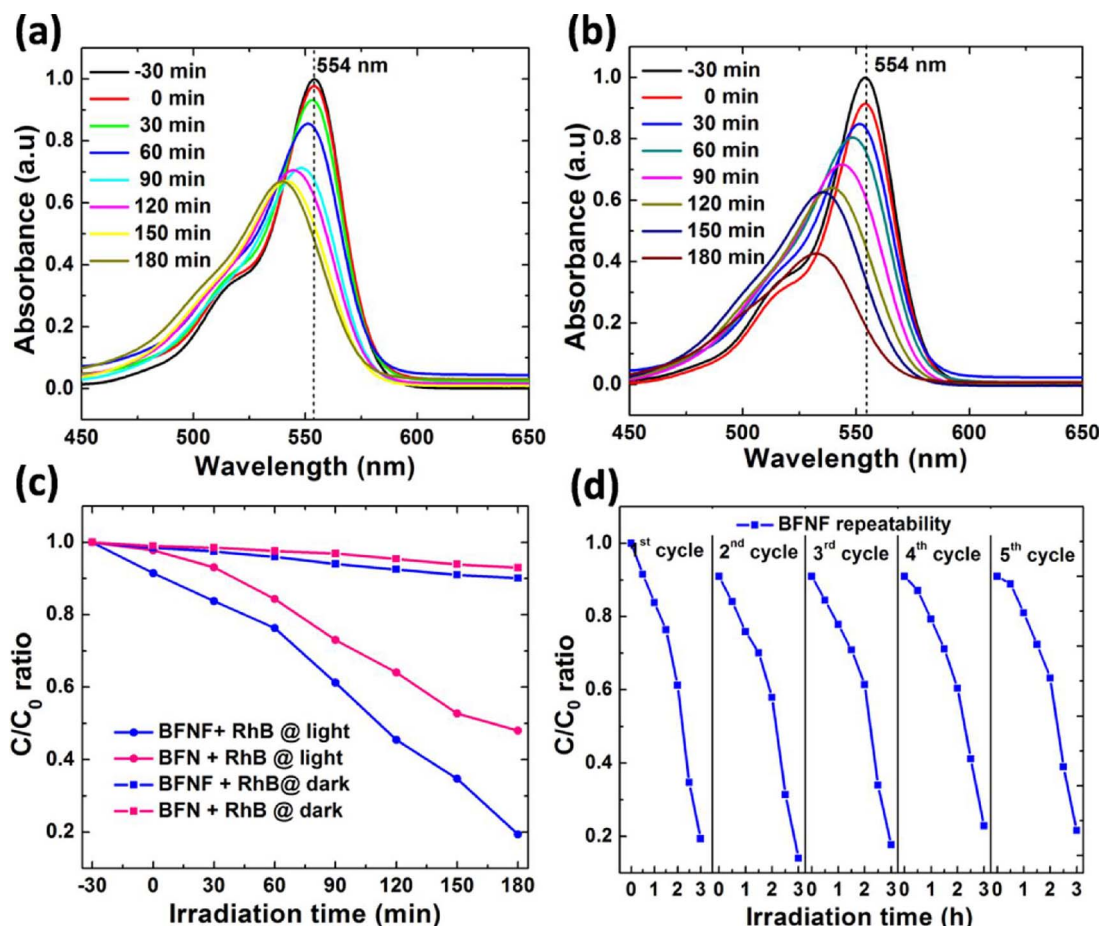
Fig. 6. Photodegradation of RhB using BFN (a), BFNF (b), rate of photodegradation of Rh B (c) and the reusability of the highly efficient BFNF NPs (d).

the arc radiuses of BFNF Nps electrode are smaller than that of the BFN electrode regardless of with or without visible-light irradiation. The smaller the arc radius of an EIS Nyquist plot implies the higher efficiency of charge separation of BFNF Nps under visible light irradiation [44]. Thus, in the case of BFNF, the photogenerated electron–hole pairs are easily separated and transferred to the sample's surface, and the photoactivities are higher than that of BFN Nps. Therefore, the enhanced photocatalytic performance is mainly attributed to the increase of the charge separation efficiency due to the broadening of the valence band (VB) width induced by asymmetric oxygen environment, which will be discussed in the following part. These results reveal the analogous trend with PL analysis and photocatalytic activity of BFNF Nps. Fig. S3 given in ESI demonstrates the cyclic voltagram of the BFNF and BFN electrodes, from which it is understood that energy corresponding to the redox potentials of BFNF are comparatively lesser than BFN, which facilitates better radical generation.

3.7.4. Active species trapping studies

The photocatalytic mechanism can be elucidated by the trapping experiments of radicals and holes. The main oxidative species in the photocatalytic process could be detected through the trapping experiments of hydroxyl radicals ($\cdot$OH), holes and superoxide radical ($\cdot O^{2-}$) by using disodium ethylenediaminetetraacetate (EDTA-2Na) ((h^+) scavenger), isopropanol (ISO) (($\cdot$OH) scavenger) and 1,4-benzoquinone (BQ) (($\cdot O^{2-}$) scavenger). Fig. 7(c) shows that the photoactivity of BFNF is greatly prevented by the addition of isopropanol, however, the addition of EDTA and BQ has only caused a change in the photodegradation which is less than isopropanol. The result suggests that the photogenerated holes are the main oxidative species of BFNF system. On the other hand, the photoactivity is also greatly inhibited by the

addition of EDTA in BFN Nps implying that the generation of holes, still all the cures are found lesser than that of BFNF Nps. This substantiates the higher photo degrading efficiency of BFNF Nps are caused by the generation of main oxidative species as OH radicals, $\cdot O^{2-}$, and holes in decreasing order.

The lattice composition dependant distorted pyrochlore structure in BFNF leads to the hybridisation of Bi 6s and Fe 3d also reduces the splitting if Nb 4d orbital and resulting a change in band edge offset [45]. Nevertheless, the perspective of distorted crystal structural dependant photocatalytic efficiency should yet to be explored in experimental and theoretical aspects that may increase the scope of Bi based pyrochlore materials to be employed as potential materials for photocatalytic water splitting applications.

4. Conclusions

In summary, pyrochlore type $Bi_{1.33}Fe_{0.052}Nb_{1.24}Fe_{1.04}O_7$ (BFNF) and $Bi_{1.34}Fe_{0.66}Nb_{1.34}O_7$ (BFN) nanoparticles (Nps) were successfully fabricated by a facile coprecipitation method. A structure refinement of the X-ray diffraction data reveal that the A-site is displaced to 96 g and O' site is displaced to 32e in cubic Fd$\bar{3}$m symmetry. The refinement result indicated that ~6% of the Fe^{3+} is misplaced on the A-site. The higher number of Raman modes together with the presence of the low wave number modes confirm the displacive nature of the BFNF Nps. Surface and morphological aspects were investigated using FESEM, HRTEM and BET which revealed that the enhanced photocatalytic efficiency in BFNF Nps are only due to the structural changes. The substantial band gap narrowing and corresponding band edge offset attributed to the displacement and/or substitution of Bi sites by Fe ions in the BFNF lattice system, which has been modeled using UV–vis DRS and valence
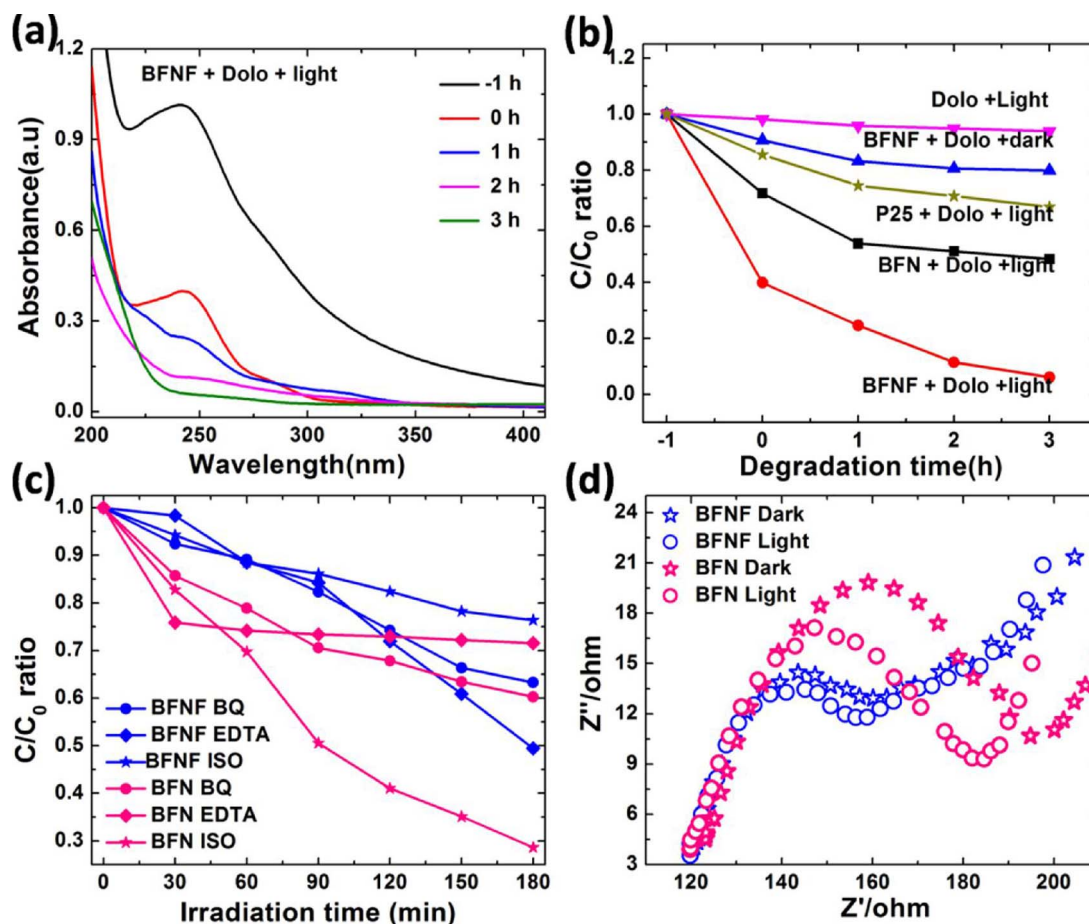
Fig. 7. (a) Photodegradation of acetoaminophen, (b) rate of photodegradation of acetoaminophen using BFNF Nps, (c) Radical trapping experiment profiles of BFNF and BFN Nps (d)EIS of BFNF and BFN Nps after deposition on ITO electrodes, with and without visible light irradiation.
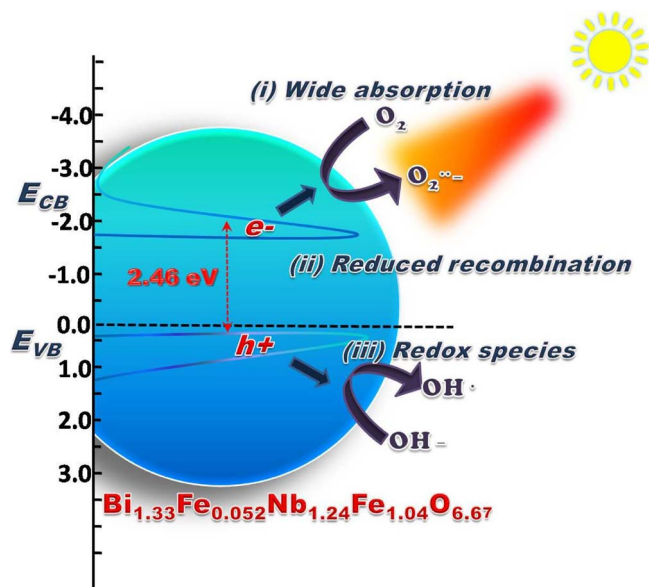

Fig. 8. Plausible mechanism of Photocatalytic degradation of Rh B using BFNF Nps.

band XPS spectra. Under visible light irradiation, BFNF Nps exhibits a much higher photocatalytic activity for degradation of RhB than BFN Nps. Based on the results of PL, EIS and active species trapping measurements, photogenerated holes (h^+) and superoxide radicals ($\cdot O_2^-$) playing a crucial role in photodegradation of RhB over BFNF Nps, the photocatalytic mechanism was proposed. The observed remarkably

improved photocatalytic activity should be resulted from the crystalline nature with controlled particle size that facilitates the effective separation and migration of the photogenerated carriers in the photocatalyst. The lattice composition dependant distorted pyrochlore structure in BFNF leads to the hybridisation of Bi 6s and Fe 3d also reduces the splitting of Nb 4d orbital resulting a change in band edge offset which is found to be more appropriate for effective photocatalysis. This synergistic effect promotes the separation and transfer of photogenerated charge carriers and simultaneously depresses the recombination of holes (h^+) and electrons (e^-), resulting in the high photocatalytic performance of BFNF Nps. The present results herein could not only provide a better understanding of the synergistic effect of Bi 6s and Fe modification but also be beneficial for the design of high performance single phase simple and efficient semiconductor photocatalysts.

Appendix A. Supplementary data

Supplementary data associated with this article can be found, in the online version, at https://doi.org/10.1016/j.apcatb.2017.12.004.

References

[1] S. Sajjad, S.A.K. Leghari, J. Zhang, RSC Adv. 3 (2013) 1363–1367.
[2] S. Bharathkumar, M. Sakar, S. Balakumar, J. Phys. Chem. C 120 (33) (2016) 18811–18821.
[3] L.Z. Pei, H.D. Liu, N. Lin, H.Y. Yu, J. Alloy Compd. 622 (2015) 254–261.
[4] R. Radha, A. Srinivasan, P. Manimuthu, S. Balakumar, J. Mater. Chem. C 3 (2015) 10285–10292.
[5] Y. Kuang, Q. Jia, H. Nishiyama, T. Yamada, A. Kudo, K. Domen, Adv. Energy Mater. 6 (2016) 1501645.
[6] Matjaz Valant, Metka Bencina, Mattia Fanetti, Acta Chim. Slov. 61 (2014) 447–452.
[7] J. Zeng, H. Wang, Y.C. Zhang, M.K. Zhu, H. Yan, J. Phys. Chem. C 111 (32) (2007) 11879–11887.
[8] A. Kudo, H. Kato, S. Nakagawa, J. Phys. Chem. 104 (3) (2000) 571–575.
[9] H.L. Tuller, Solid State Ionics 52 (1–3) (1992) 135–146.
[10] M.P. Vandijk, A.J. Burggraaf, A.N. Cormack, C.R.A. Catlow, Solid State Ionics 17 (2) (1985) 159–167.
[11] H. Zhang, M. Lü, S. Liu, X. Song, Y. Zhou, Z. Xiu, Z. Qiu, A. Zhang, Q. Ma, Thin Solid Films 517 (2008) 764–768.
[12] W.F. Yao, H. Wang, X.H. Xu, J.T. Zhou, X.N. Yang, Y. Zhang, S.X. Shang, Appl. Catal. A 259 (2004) 29–33.
[13] Q. Xiao, Q. Zhou, J. Zhang, L. Ouyang, J. Alloys Compd. 468 (2009) L9–L12.
[14] D. Pei, J. Luan, Int. J. Photoenergy 2012 (2012) 1.
[15] V.M. Sharma, D. Saha, G. Madras, T.N.G. Row, RSC Adv. 3 (2013) 18938–18943.
[16] L.M. Torres-Martínez, M.A. Ruiz-Gómez, M.Z. Figueroa-Torres, I. Juárez- Ramírez, E. Moctezuma, Int. J. Photoenergy 2012 (2012) 1.
[17] D.M. De los Santos, J. Navas, T. Aguilar, A. Sánchez-Coronilla, C. Fernández-Lorenzo, R. sAlcántara, J. Carlos Piñero, G. Blanco, J. Martín-Calleja, Beilstein J. Nanotechnol. 6 (2015) 605–616.
[18] D. Saha, G. Madras, T.N. Guru Row, Dalton Trans. 41 (2012) 9598–9600.
[19] H. Xue, Y. Zhang, J. Xu, X. Liu, Q. Qian, L. Xiao, Q. Chen, Catal. Commun. 51 (2014) 72–76.
[20] W. Miller, L. Causeret, C.D. Ling, J. Phys.: Condens. Matter 22 (2010) 486004.
[21] J.A. Pedraza-Avella, K.L. Rosas-Barrera, J.E. Pedraza-Rosas, D.A. Laverde-Cataño, Top. Catal. 54 (2011) 244–249.
[22] W. Somphon, V. Ting, Y. Liu, R.L. Withers, Q. Zhou, B.J. Kennedy, J. Solid State Chem. 179 (2006) 2495–2505.
[23] L. Garza-Tovar, L.M. Torres-Martinez, D.B. Rodriguez, R. Gomez, G. del Angel, J. Mol. Catal. A 247 (2006) 283–290.
[24] M.W. Lufaso, T.A. Vanderah, I.M. Pazos, I. Levin, R.S. Roth, J.C. Nino, V. Provenzano, P.K. Schenck, J. Solid State Chem. 179 (2006) 3900.
[25] Metka Bencina, Matjaz Valant, Michael W. Pitchera, Mattia Fanettiac, Nanoscale 6 (2014) 745–748.
[26] V. Krayzman, I. Levin, J.C. Woicik, Chem. Mater. 19 (2007) 932–936.
[27] M. Avdeev, M.K. Haas, J.D. Jorgensen, R.J. Cava, J. Solid State Chem. 169 (2002) 24–34.
[28] Raja Altaf U. Rahman, Peter Schmid-Beurmann, Ramaswamy Murugan, J. Mater. Chem. C 4 (2016) 7766–7774.
[29] Alejandro Gómez-Pérez, Jesús Prado-Gonjal, Daniel Muñoz-Gil, Adrián AndradaChacón, Javier Sánchez-Beńıtez, Emilio Morán, Maŕıa Teresa Azcondo, Ulises Amadora, Rainer Schmidt, RSC Adv. 5 (2015) 85229–85241.
[30] G. Perenlei, P.C. Talbot, W.N. Martens, J. Nanomater. 2014 (2014) 6.
[31] T.A. Vanderah, M.W. Lufaso, A.U. Adler, I. Levin, J.C. Nino, V. Provenzano, P.K. Schenck, J. Solid State Chem. 179 (2006) 3467–3477.
[32] I. Bryntse, Eur. J. Solid State Inorg. Chem. 28 (2) (1991) 481.
[33] Gunda Santosh Babu, Matjaz Valant, Katharine Page, Anna Llobet, Taras Kolodiazhnyi, Anna-Karin Axelsson, Chem. Mater. 23 (2011) 2619–2625.
[34] Ganchimeg Perenlei, Jose A. Alarco, Peter C. Talbot, Wayde N. Martens, Synth. Int. J. Photoenergy 2015 (2015) 11.
[35] I. Levin, T.G. Amos, J.C. Nino, T.A. Vanderah, C.A. Randall, M. Lanagan, J. Solid State Chem. 168 (2002) 69–75.
[36] T.A. Vanderah, I. Levin, M.W. Lufaso, An unexpected crystal-chemical principle for the pyrochlore structure, Eur. J. Inorg. Chem. (2005) 2895–2901.
[37] K. Sardar, S.C. Ball, J.D.B. Sharman, D. Thompsett, J.M. Fisher, R.A.P. Smith, Pabitra K. B, Martin R. L, R.J. Kashtiban, Jeremy Sloan, Richard I. Walton, Chem. Mater. 24 (21) (2012) 4192–4200.
[38] Chehreh Chelgani, B. Hart, M. Biesinger, J. Marois, M. Ourriban, Miner. Eng. 55 (2014) 165–171.
[39] Wei Sun, Ji-Yuan Liu, Xue-Qing Gong, Waqas-Qamar Zaman, Li-Mei Cao, Ji Yang, Sci. Rep. 6 (2016) 38429.
[40] S. Ponce, M.A. Peña, J.L.G. Fierro, Appl. Catal. B: Environ. 24 (2000) 193–205.
[41] C. Pan, D. Zhang, L. Shi, J. Solid State Chem. 181 (2008) 1298–1306.
[42] Y.H. Lv, W.Q. Yao, X.G. Ma, C.S. Pan, R.L. Zong, Y.F. Zhu, Catal. Sci. Technol. 3 (12) (2013) 3136–3146.
[43] Santosh K. Gupta, K. Sudarshan, P.S. Ghosh, A.P. Srivastava, S. Bevara, P.K. Pujari, R.M. Kadam, J. Mater. Chem. C 4 (2016) 4988.
[44] D.M. Adams, Inorganic Solids: An Introduction to Concepts in Solid-State Structural Chemistry, John Wiley, London, 1974.
[45] Chris E. Mohn, Svein Stølen, Phys. Rev. B 83 (2011) 014103.
[46] A. Kudo, Y. Miseki, Chem. Soc. Rev. 38 (2009) 253–278.
[47] J. Zhou, M. Zhang, Y. Zhu, Phys. Chem. Chem. Phys. 17 (2015) 3647–3652.
[48] Jason K. Cooper, Sheraz Gul, Francesca M. Toma, Le Chen, Yi-Sheng Liu, Jinghua Guo, Joel W. Ager, Junko Yano, Ian D. Sharp, J. Phys. Chem. C 119 (2015) 2969–2974.
[49] Wenjie Fan, Jinli Hu, Jing Huang, Xin Wu, Sen Lin, Caijin Huang, Xiaoqing Qiu, Appl. Surf. Sci. 357 (2015) 2364.